# Kinematic study of O⁻-ion formation from dissociative electron attachment to SO₂

Irina Jana and Dhananjay Nandi*

*Department of Physical Sciences, Indian Institute of Science Education and Research, Kolkata, Mohanpur 741246, India*
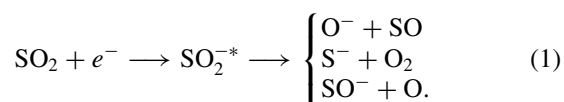
We report a complete kinematic study of O⁻-ion formation due to dissociative electron attachment to SO₂ using the velocity slice imaging technique in the incident electron energy range over the resonances. Two resonances are observed at 5.2 and 7.5 eV, respectively. From the kinetic energy distribution, the two resonances are observed to have the same threshold energy, pointing to the fact that the two processes, giving rise to the two resonant peaks, have the same dissociation limit. From the angular distribution results we identified the involvement of an $A_1$ and a combination of $A_1 + B_2$ temporary negative-ion state(s) for the first and second resonances, respectively.

## I. INTRODUCTION

Dissociative electron attachment (DEA) can be considered to be a two-step process where a single low-energy ($\leqslant 15$ eV) electron first gets captured by a molecule, hence forming a resonance. The singly charged molecular anion thus formed is called the temporary negative ion (TNI). This TNI may then dissociate, giving a negative ion and one (or more) neutral fragment(s). The stability of the neutral molecule may drastically change due to its transition from a neutral to a negative molecular ion. The particular molecular orbital (MO) where the electron gets attached and the energy of the incoming electron determine the amount of internal energy and the way this energy is deposited in the molecule. DEA resulting in formation of negative ions is one of the basic processes in the upper atmosphere, interstellar space, plasmas, and various other processes, including many methods of mass spectrometry [1]. Study of these negative-ion states also gives a knowledge of their role in radiation damage [2] and site-specific fragmentation, helping in controlling chemical reactions [3].

SO₂ is a triatomic molecule with $C_{2v}$ symmetry. SO₂ is one of the most abundant pollutants of the atmosphere, especially in cities and areas of large factories, industries, and power plants [4]. Pulsed ion lasers are also known to use SO₂ as a source of sulfur ions [5]. Hence the study of SO₂ molecules can be of immense interest. The molecule has 18 valence electrons with a ground-state molecular orbital configuration $(7a_1)^2, (1a_2)^2, (4b_2)^2, (8a_1)^2$ and a permanent dipole moment of 1.63305 D [6–8]. DEA to SO₂ is commonly known to take place via the following pathways:

$$\mathrm{SO_2} + e^- \longrightarrow \mathrm{SO_2^{-*}} \longrightarrow \begin{cases} \mathrm{O^-} + \mathrm{SO} \\ \mathrm{S^-} + \mathrm{O_2} \\ \mathrm{SO^-} + \mathrm{O}. \end{cases} \tag{1}$$

Back in 1970, Rallis and Goodings performed DEA measurement to two triatomic molecules, namely, SO₂ and NO₂, using a trapped electron apparatus and reported the ion yield curve and kinetic energy of the negative ion as a function of

incident electron energy [9]. Studies reporting attachment of low-energy electrons to SO₂ in high-pressure gases like N₂, C₂H₄, and Ar were also known in the year 1974 [6]. There have been many studies reporting the dissociative attachment cross sections of O⁻, S⁻, and SO⁻ ions from DEA to both ground and excited states of SO₂ for the last few decades [5,10]. Vinodkumar *et al.* have calculated the total cross section for $e - \mathrm{SO_2}$ scattering using the *ab initio R*-matrix method over a wide energy range of 0.1–2000 eV [11].

Previous experimental studies have shown to produce O⁻, S⁻, and SO⁻ ions from DEA to SO₂, each having two prominent peaks in the ion yield curve [10,12]. The first peak is observed between 4 and 5 eV, while the second peak is at an energy slightly above 7 eV. An additional small peak at around 9 eV is reported for S⁻/SO₂ [5,13].

By performing *ab initio* molecular orbital calculations for the ground state of a neutral SO₂ molecule, Krisnakumar *et al.* in 1996 suggested the first peak at 4.6 eV to be due to a $^2A_1$ negative-ion resonant state and the second peak at 7.3 eV due to a $^2B_2$ negative-ion resonant state [7]. The next year in 1997, Krishnakumar *et al.* measured the absolute cross section of ground and excited states of SO₂ and, based on selection rules for dissociative attachment, stated the first two resonances at 4.6 and 7.5 eV to be due to $^2A_1$ and $^2B_2$ negative-ion resonant states, respectively [10], while the third resonance at 9 eV for S⁻/SO₂ ions was suggested to be due to any one among $^2A_1$ or $^2B_1$ or $^2B_2$ states. Gupta and Baluja also reported the presence of three resonant states at 4.50, 6.25, and 9.58 eV for DEA to SO₂ using the *R*-matrix method [13]. They identified the presence of bound state of SO₂⁻ in $^2B_1$ symmetry. The $^2A_1$, $^2B_2$ states are reported as shape resonances with $^2B_2$ symmetry corresponding to the first resonant peak, while the $^2A_2$, $^2B_1$ symmetries are due to core-excited shape resonances, with 6.25 eV being the first core-excited resonance. But no angular distribution data was reported in support of the above made claims. Recently, Gope *et al.* reported the kinetic energy release for O⁻, SO⁻, and S⁻ channels for the two resonant peaks stating that the O⁻ and SO⁻ ions occur due to an asymmetric dissociation of the parent anion, while the S⁻ ions are formed due to a symmetric dissociation [14]. Gope *et al.* also gave the angular distribution for only SO⁻ ions at 6.9-eV incident

───────
*dhananjay@iiserkol.ac.in

electron energy and suggested a contribution of $B_1$ and $B_2$ states from the fitted angular distribution data.

In this article we report a complete kinematic study of $O^-$ ion formation from DEA to $SO_2$ around the first and second resonant peaks observed at 5.2 and at 7.5 eV, respectively. The measurements have been performed using the velocity map imaging (VMI) spectrometer [15]. The velocity slice imaging (VSI) technique is a sophisticated tool for the simultaneous measurement of kinetic energy and angular distribution over the entire $2\pi$ angle with higher efficiency [16]. Using the VSI technique we report the kinetic energy distribution of $O^-$ ions for the 5.2- and 7.5-eV resonances. We also report the angular distribution of $O^-$ ions and give a clear evidence for the presence of the $A_1$ state for the first resonance and $B_2$ state for the second resonance, in agreement with previous studies [7,10]. Based on the fitted angular distribution data, we also propose the presence of the $A_1$ state along with the $B_2$ state for the 7.5-eV resonance. The presence of the $A_1$ state for the 7.5-eV resonance has not been reported earlier.

## II. INSTRUMENTATION

The experiments are performed probing the well-established velocity map imaging technique. The VMI spectrometer along with the other experimental details has been discussed elaborately in previous work [15]. It employs a magnetically collimated pulsed electron beam coming from a homemade electron gun crossed with an effusive molecular beam coming from a capillary tube. The electron gun has a filament which works on the fundamental thermionic emission process, having a resolution of about 0.8 eV. A pair of magnetic coils in Helmholtz configuration is mounted outside the chamber to produce a uniform magnetic field in the interaction region. The ions produced in the interaction region form a "Newton sphere." The electron-gun pulse has a width of 200 ns with 10-kHz repetition rate. The base pressure is of the order of $10^{-9}$ mbar and of the order of $10^{-7}$ mbar with the molecular beam. After the ions are produced, the Newton sphere is pushed from behind by applying a 4-$\mu$s pulse at the pusher plate after a delay of 100 ns from the electron-gun pulse. This delay ensures the extraction for better slice images. The Newton spheres then move through the puller, lens electrode, and enter the 110-mm-long field-free flight tube. The Newton spheres expand freely in the flight tube and finally fall on the position sensitive detector (PSD). The PSD consists of three microchannel plates (MCPs) placed in a Z-stack configuration and a delay-line hexanode [17]. Ions with a given velocity map onto a single point on the detector irrespective of the place of birth. The time-of-flight (TOF) of the detected ions can be determined from the signal taken from the back plate of the MCP, while the $x$, $y$ position coordinates can be known from the signals obtained from the hexanode. The TOF and $x$, $y$ position coordinates data are stored in a list-mode file (LMF) format using the CoboldPC software from Roentdek. The time-slice images with suitable time window can be analyzed off-line from the LMF format using the same CoboldPC software. The central slice contains kinematically complete information, including kinetic energy release and angular distribution of the detected ions.
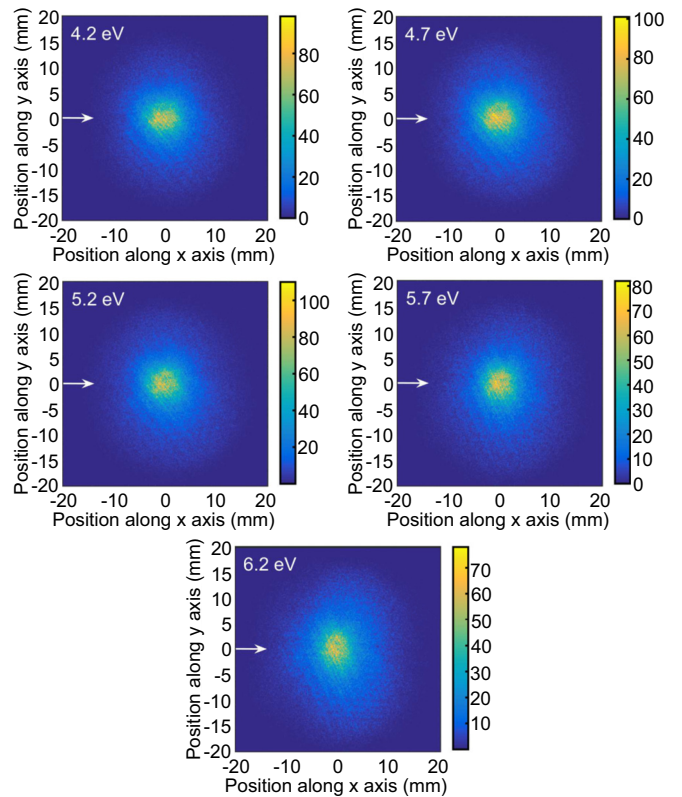


FIG. 1. Time-slice images of $O^-$ ions at different incident electron energies around the first resonance. The arrows indicate the direction of the incident electron beam.

The system is first optimized by performing DEA to $O_2$ where $O^-$ ions are observed, forming a single resonance at 6.5 eV. The $SO_2$ and $O_2$ gases used for the experiment, with a stated purity of 99.99%, are obtained from PRAXAIR.

## III. RESULTS AND DISCUSSIONS

The central time-slice images measured around the first resonance at incident electron energies of 4.2, 4.7, 5.2, 5.7, and 6.2 eV are shown in Fig. 1. Closer inspection shows a central blob of ions which increases in size with incident electron energy. The time-slice images of the central slice measured around the second resonance at incident energies 6.5, 7.0, 7.5, 8.0, 8.5, and 9.0 eV are shown in Fig. 2. It can be noted from the time-slice images that for 6.5-, 7.0-, 7.5-, and 8.0-eV incident electron energies, there is a single central circular blob of ions with almost uniform distribution. But for 8.5-eV incident electron energy, the central blob starts separating out into two lobes. At 9.0-eV incident electron energy, the two lobes further increase in size and become more distinct.

### A. Kinetic energy distribution

The kinetic energy distributions are obtained by integrating over the entire ejection angle of the respective negative ions ($O^-$ ions in this case) and then plotting the normalized ion counts as a function of ion kinetic energy. From energy and momentum conservation, the kinetic energy of the negative
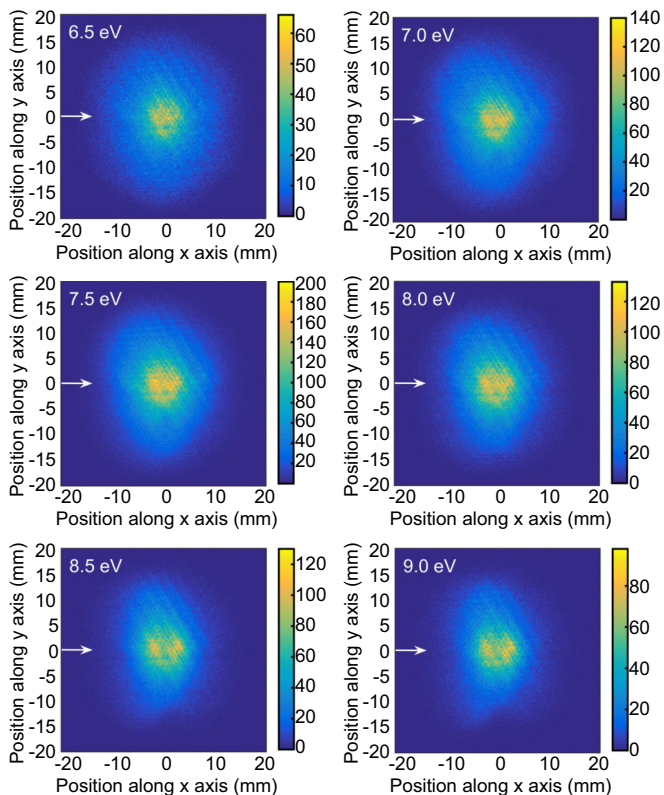
FIG. 2. Time-slice images of O⁻ ions at different incident electron energies around the second resonance. The arrows indicate the direction of the incident electron beam.

ion can be written as

$$E_R = \left(1 - \frac{m}{M}\right)[V_e - (D - A + E^*)], \qquad (2)$$

where $m$ is the mass of negative ion, $M$ is the mass of neutral $SO_2$ molecule, $V_e$ is the incident electron energy, $D$ is the bond dissociation energy, $A$ is the electron affinity of the negative-ion fragment, and E* is the excitation energy of the neutral fragment formed after dissociation [15].

### First resonance at 5.2 eV

The kinetic energy distributions for incident electron energies of 4.2, 4.7, 5.2, 5.7, and 6.2 eV are shown in Fig. 3. The kinetic energy distributions show a single peak near 0 eV for all the incident electron energies. The kinetic energy distributions of the negative-ion fragment O⁻ and the internal energy of the neutral fragment SO can be determined from the slice images, assuming the DEA process is a two-body breakup. The threshold for O⁻/SO₂ formation being 4.145 eV [9], it can be predicted that the excess 1.06-eV (= 5.2–4.14 eV) energy gets distributed among the fragments' translational and internal energies. The kinetic energy peak at around 0 eV implies that most of the excess energy gets used up for rotational and vibrational excitation. In a recent study of O⁻ ions from DEA to SO₂, Gope *et al.* reported that the neutral SO fragment is produced with very little kinetic energy in the ground electronic state, implying a vibrational excitation of the SO fragment [14]. The inset shows that with the increase in
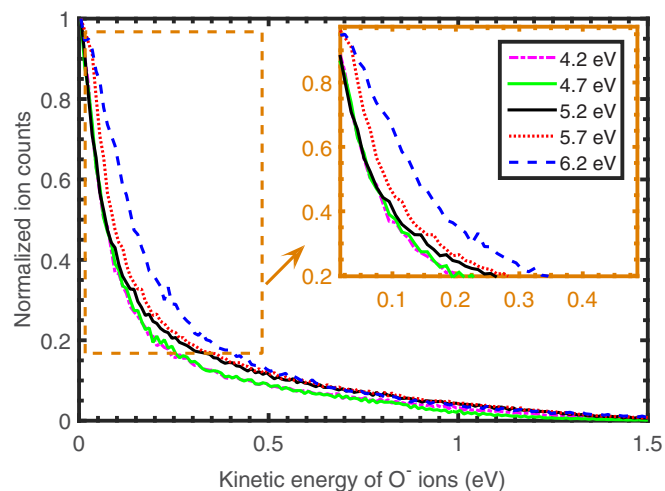


FIG. 3. The unweighted kinetic energy distribution of the O⁻ ions created due to interaction with different incident electron energies at the first resonance. The number of counts is normalized at the near zero eV peak value.

incident electron energy the distributions shift to higher kinetic energies, which is depicted by an increase in the distribution width. This increase may be due to an overall increase in rotational, vibrational, and translational kinetic energies.

### Second resonance at 7.5 eV

The kinetic energy distributions for incident electron energies of 6.5, 7.0, 7.5, 8.0, 8.5, and 9.0 eV are shown in Fig. 4. The kinetic energy distributions show a single peak near 0 eV for incident electron energies of 6.5–8.0 eV, implying most of the ions are produced with energies near 0 eV. For 8.5-eV incident electron energy, it can be observed that the peak of the kinetic energy distribution is no longer at 0 eV but slightly shifted rightwards. This shift indicates that with the increase
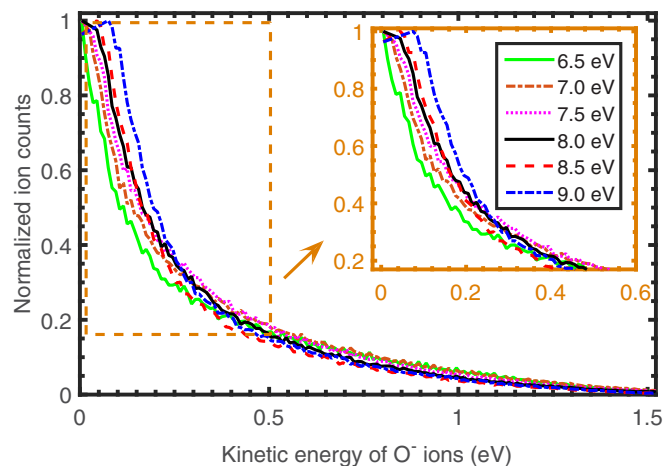


FIG. 4. The unweighted kinetic energy distribution of the O⁻ ions created due to interaction with different incident electron energies at the second resonance. The number of counts is normalized at the near zero eV peak value.
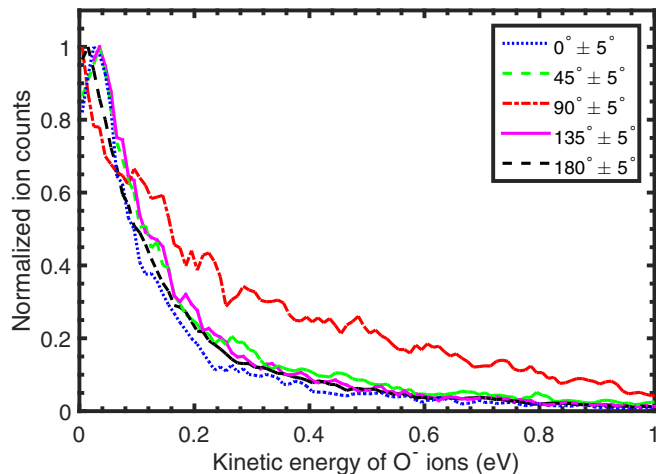
FIG. 5. The kinetic energy distribution at different ejection angles at 9.0-eV incident electron energy.



FIG. 6. The most probable kinetic energy versus incident electron energy curve of $O^-$ ions created due to the two-body breakup. The first two data points having almost the same energy as the third are not shown in the figure for a better fit. The linear fit for the data is also shown. The fitted line intersects the x-axis at 3.1 eV.

in electron energy, the counts in the center of the time-slice images decreases and the maximum number of counts shifts to some higher energy denoted by larger radius in the time-slice images (Fig. 2). The same happens for 9.0-eV incident electron energy with the shift being even higher. This in turn points to the fact that the central blob starts separating into two lobes.

Figures 3 and 4 show the plot of kinetic energy distribution for $O^-$ ions for the first and second resonance, respectively, at an entire $2\pi$ ejection angle. However, it is also interesting to see the kinetic energy distribution at different ejection angles with respect to the incident electron beam. One such example is shown in Fig. 5 for 9.0-eV incident electron energy for ejection angle ranges $0° \pm 5°$, $45° \pm 5°$, $90° \pm 5°$, $135° \pm 5°$, and $180° \pm 5°$, where the central blob has already separated into two lobes. It can be noted from the figure that the kinetic energy distribution varies with change in ejection angle. For $90° \pm 5°$, the distribution has a peak at 0-eV energy, while for $0° \pm 5°$, $45° \pm 5°$, $135° \pm 5°$, and $180° \pm 5°$, the kinetic energy distribution peak is shifted from 0 eV. This is also evident from the time-slice images (Fig. 2).

### Plot of threshold energy curve

The plot of kinetic energy of $O^-$ ions versus incident electron energy for both the resonances is shown in Fig. 6. Linear fit to the data points and extrapolation to the x axis gives the threshold energy for the process. The straight line cuts the x axis at 3.1 eV. The thermochemical threshold value being 4.145 eV [9], the experimental value is found to match well with theory considering the 0.8-eV energy resolution of the electron gun. If all the excess energy was distributed as the kinetic energy of the fragments, then the slope would have been 0.75 [18]. But the observed slope of 0.082 signifies the vibrational and rotational excitation of the neutral SO fragment. One very important conclusion can be drawn from this plot. For both the resonances at 5.2 and 7.5 eV, there is only one threshold energy. This implies there is only one dissociation limit for both the resonances. The two distinct anion resonances, having different electron attachment
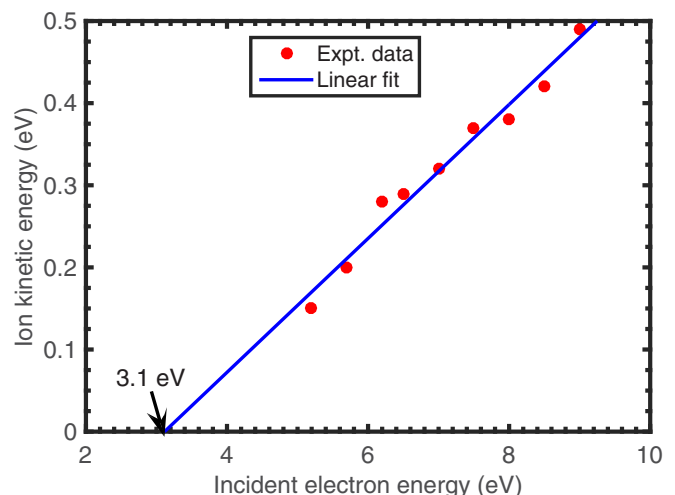
(vertical) thresholds but with the same adiabatic dissociation threshold, also implies that there could be a nonadiabatic coupling between the two resonances. However, a time-dependent nuclear dynamics would be helpful for this clarification, which is beyond the scope of this work. Our data matches very well with the threshold energy plot reported by Nandi and Krishnakumar [18]. Nandi and Krishnakumar measured the kinetic energy of $O^-$ ions using the time-of-flight technique where the time-of-flight spectra were measured at different incident electron energies. For each spectra the zero in the time axis denoted ions with zero kinetic energy. "Direct ions" were indicated with negative times and "turn-around ions" with positive times. Thus the contribution of ions originating mainly around $90°$ was taken into account. But the formation of lobes from 8.5-eV incident electron energies onwards shows that the distribution has a very low count at $90°$. Instead, the count starts increasing at around $0°$ and $180°$. With the help of the present VMI spectrometer, kinetic energy and angular distributions of ions originating at the entire $2\pi$ angle could be measured and accounted for.

### B. Angular distribution

The SO$_2$ molecule has a $C_{2v}$ symmetry. The ground-state molecular orbital (MO) configuration is $(7a_1)^2,(1a_2)^2,(4b_2)^2,(8a_1)^2$ making an overall $\tilde{X}\,^1A_1$ state [7].

The generic formula for angular distribution of diatomic molecules as given by O'Malley and Taylor can be written as [19]

$$f(k,\theta,\phi) \approx \Sigma_{|\mu|}\left|\Sigma_{l=|\mu|}^{\infty}a_{l\mu}(k)Y_{l\mu}(\theta,\phi)\right|^2, \qquad (3)$$

where $k$ is the incident electron momentum, $a_{l\mu}$ are the energy-dependent expansion coefficients, $Y_{l\mu}(\theta,\phi)$ are the spherical harmonics, $\mu = |\bigwedge_f - \bigwedge_i|$ represents the difference in projection of electronic orbital angular momentum along the

TABLE I. $C_{2v}$ group table and basis functions.

|       | I | $C_2$ | $\sigma_v$ | $\sigma_v'$ | Basis functions |
|-------|---|-------|------------|-------------|-----------------|
| $A_1$ | 1 | 1 | 1 | 1 | $Y_l^0$ or $Y_l^m + Y_l^{-m}$, $m$ even |
| $A_2$ | 1 | 1 | −1 | −1 | $Y_l^m - Y_l^{-m}$, $m$ even |
| $B_1$ | 1 | −1 | −1 | 1 | $Y_l^m + Y_l^{-m}$, $m$ odd |
| $B_2$ | 1 | −1 | 1 | −1 | $Y_l^m - Y_l^{-m}$, $m$ odd |

molecular axis for the final and initial states, respectively, $l$ is the orbital angular momentum of the incoming electron for $l \geqslant \mu$ values, and $(\theta, \phi)$ are the polar angles.

The modified expression for polyatomic molecules as given by Azria *et al.* for angular distribution in the laboratory frame by averaging over the angle $\phi$ can be written as [20]

$$f(\theta) \propto \frac{1}{2\pi} \int_0^{2\pi} \left| \Sigma_{l,m,\varepsilon} i^l \exp(i\delta_l) a_{lm}^\varepsilon X_{lm}^{\varepsilon*}(\theta,\phi) \right|^2 d\phi. \quad (4)$$

Following the procedure given by Azria *et al.*, the amplitudes for the transition from $A_1$ to $A_1$, $A_2$, $B_2$ and $B_2$ negative-ion states can be found out. The ground state of the neutral $SO_2$ molecule given by $A_1$ can be represented by the basis function $Y_0^0$. The basis functions for the $C_{2v}$ symmetry group are shown in Table I [21]. The transition amplitude can be written as

$$f(\theta,\phi) = \langle \text{Final state}|\text{Partial wave}|\text{Initial state}\rangle \quad (5)$$

where the initial state, final state, and partial waves are represented by the spherical harmonics after necessary transformation by Euler angles for molecular frame along the dissociation axis. The scattering intensity is finally given by

$$I(\theta) = \int_0^{2\pi} |f(\theta,\phi)|^2 d\phi. \quad (6)$$

The equations for $A_1$ to $A_1$ transitions due to a $p$, combination of $(s + p)$, and $(s + p + d)$ partial waves are given below [21]:

$I_p(\theta) = \sin^2 \beta \sin^2 \theta + 2 \cos^2 \beta \cos^2 \theta,$

$I_{s+p}(\theta) = a^2 + b^2(\sin^2 \beta \sin^2 \theta + 2 \cos^2 \beta \cos^2 \theta) + 4ab \cos \beta \cos \theta \cos \delta,$

$I_{s+p+d}(\theta) = a^2 + b^2(\sin^2 \beta \sin^2 \theta + 2 \cos^2 \beta \cos^2 \theta) + c^2[\frac{9}{16}(\sin^4 \beta \sin^4 \theta + \sin^2 2\beta \sin^2 2\theta) + \frac{1}{2}(3\cos^2 \beta - 1)(3\cos^2 \theta - 1)] + 4ab \cos \beta \cos \theta \cos \delta_1 + 2bc[\frac{3}{4}\sin \beta \sin 2\beta \sin \theta \sin 2\theta + \frac{1}{2}\cos \beta(3\cos^2 \beta - 1)\cos \theta(3\cos^2 \theta - 1)]\cos \delta_2 + ac(3\cos^2 \beta - 1)(3\cos^2 \theta - 1)\cos(\delta_1 + \delta_2),$

where the letters $a$, $b$, and $c$ represent fitting parameters, $\delta$'s arise due to the difference between the phases of two partial waves from potential scattering, and $\beta$ is a Euler angle representing the angle between the molecular symmetry axis and the dissociating O-S bond.

The partial-wave analysis used in this article assumes that the axial recoil approximation holds, i.e., there is no significant rotation of the internal coordinates of the transient negative ion. However, it has been observed in the extant literature of DEA to polyatomic molecules such as $NF_3$ [22] and $CO_2$ [23], where the transient negative ion undergoes significant bending, resulting in change of its symmetry group, signaling a strong
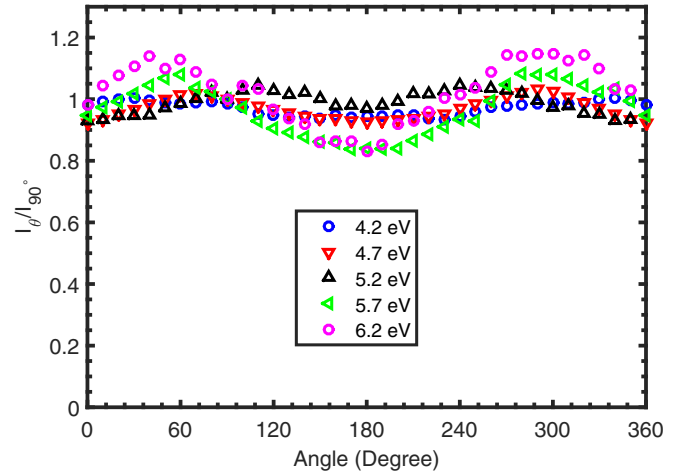


FIG. 7. Angular distribution of the O⁻ ions having kinetic energy between 0 and 0.5 eV for all the five incident electron energies around the first resonance.

breakdown of the axial recoil approximation. In the present article, *ab initio* calculations have been performed, which shows that the transient negative ion formed after electron attachment changes very little from its neutral state. The bond angle decreases by 4.7°, while the bond length increases by 0.08 Å, retaining the $C_{2v}$ symmetry. Thus, even if there is a slight change in the TNI, owing to the coupled nature of the two resonances leading to the same dissociation state, the axial recoil approximation holds and thus the partial-wave analysis is still applicable for the present study.

**First resonance at 5.2 eV**

The angular distribution data for O⁻ ions over the kinetic energy range 0–0.5 eV measured at incident electron energies of 4.2, 4.7, 5.2, 5.7, and 6.2 eV are shown in Fig. 7. As can be observed from the figure, at 4.2-eV incident electron energy, the distribution is nearly isotropic in nature, but with the increase in incident electron energy, the nature starts changing slowly. For all the incident electron energies the curves are symmetric at about 180° with a relative change in intensity.

The angular distribution curves are fitted with spherical harmonics corresponding to $A_1$ to $A_1$, $A_1$ to $A_2$, $A_1$ to $B_1$, $A_1$ to $B_2$ transitions, and also combination of more than one state by a linear superposition of spherical harmonics [21]. But the best fit was observed for the $A_1$ to $A_1$ transition with $R^2$ value around 0.9 at resonance (Fig. 8). The first three partial waves that contribute to the $A_1$ state are $s$, $p$, and $d$ waves, where the $s$ wave is most dominant. This makes us conclude that the first resonant peak at 5.2 eV occurs due to the presence of the $A_1$ negative-ion state, which is in accordance with previous studies [7,10]. The amplitudes of these contributing partial waves may undergo interference, producing forward-backward asymmetry. The ratio of different fitting parameters and phase differences along with $R^2$ value are given in Table II for the first resonance at around 5.2-eV incident electron energy.
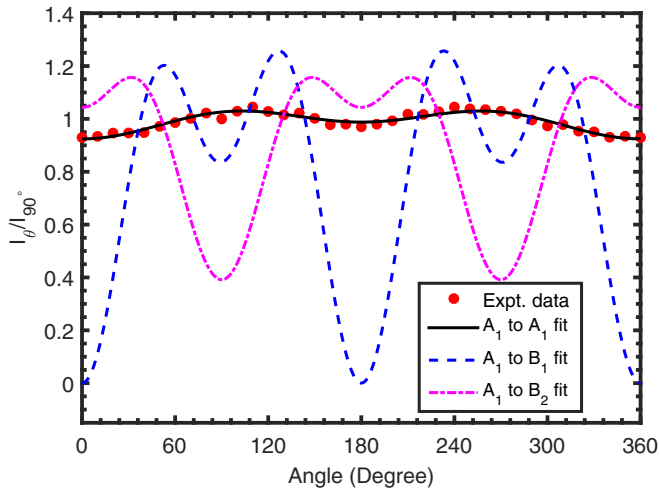
FIG. 8. Fit to the angular distribution data of the $O^-$ ions for 5.2-eV incident electron energy at the first resonance. The black solid line denotes the fit for the $A_1$ to $A_1$ transition, the blue dashed line denotes fit for the $A_1$ to $B_1$ transition, and the pink dash-dotted line denotes fit for the $A_1$ to $B_2$ transition.
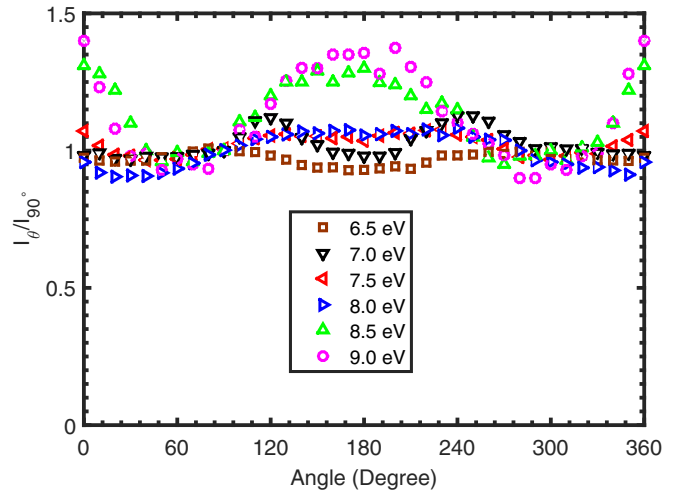


FIG. 9. Angular distribution of the $O^-$ ions having kinetic energy between 0 and 0.2 eV for all the six incident electron energies around the second resonance.

### Second resonance at 7.5 eV

The angular distribution data for $O^-$ ions over the kinetic energy range 0–0.2-eV measured at incident electron energies 6.5, 7.0, 7.5, 8.0, 8.5, and 9.0 eV are shown in Fig. 9. From the time-slice images (Fig. 2) it can be observed that as the central blob separates into two lobes, the distribution peaks at around $0°$ and $180°$. This feature of the angular distribution can be understood clearly from the angular distribution data (Fig. 9). There are two distinct peaks for the incident electron energies at 6.5 and 7.0 eV. These peaks come closer for incident electron energies of 7.5 and 8.0 eV and finally merge together, forming a broad peak near $180°$ and two peaks near $0°$ and $360°$ for incident electron energies 8.5 and 9.0 eV.

According to previous reports [7,10], the second resonance at 7.5 eV is due to the $B_2$ negative-ion state, but from our angular distribution data we could find that only the $A_1$ to $B_2$ transition did not give a good fit. The best fit is obtained for the $A_1$ to $A_1 + B_2$ transition (Fig. 10). The first three partial waves that contribute to the $A_1$ state are $s$, $p$, and $d$ waves, while the first two partial waves contributing to the $B_2$ state are $p$ and $d$ waves. For the 7.5-eV incident electron energy, the $p$ wave is most dominant for both the $A_1$ and $B_2$ states.

This implies that the second resonant peak at 7.5 eV occurs due to the presence of $A_1$ and $B_2$ negative-ion states. The fit to the 9.0 eV angular distribution data also shows that an $A_1$ to $A_1 + B_2$ transition is responsible for the distribution, with $s$, $p$, and $d$ waves contributing to the $A_1$ state, while $p$ and $d$ waves contribute to the $B_2$ state (Fig. 10). In this case the $s$ wave plays the most dominant role for the $A_1$ state and $p$ wave for the $B_2$ state. The fit becomes even better as compared to the 7.5-eV resonance fit considering the $R^2$ value. The ratio of different fitting parameters and phase differences along with $R^2$ values for the 7.5- and 9.0-eV incident electron energies are given in Table III.

TABLE II. Fitting parameters for angular distribution of $O^-$ ions for $A_1$ to $A_1$ transition.

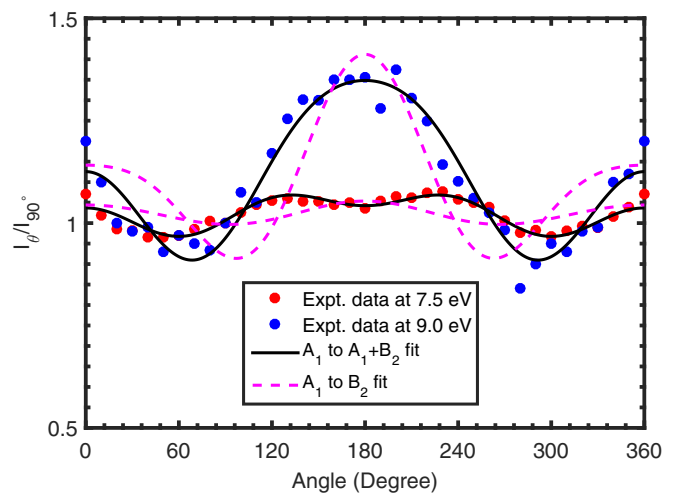| | 5.2-eV incident energy |
|---|---|
| Weighing ratio of partial waves | |
| $a : b : c$ | $1 : 0.01 : 0.01$ |
| Parameter | |
| $\beta, \delta_1, \delta_2$ | 0.33, 6.83, 9.48 |
| $R^2$ | 0.91 |



FIG. 10. Fit to the angular distribution data of the $O^-$ ions for 7.5- and 9.0-eV incident electron energies around the second resonance. The black solid line denotes the fit for the $A_1$ to $A_1 + B_2$ transition and the pink dashed line denotes fit for the $A_1$ to $B_2$ transition.

TABLE III. Fitting parameters for angular distribution of $O^-$ ions for $A_1$ to $A_1 + B_2$ transition.

| | 7.5-eV incident energy | 9.0-eV incident energy |
| --- | --- | --- |
| Weighing ratio partial waves | | |
| $a : b : c : d : e$ | 0.04 : 1 : 0.04 : 0.98 : 0.08 | 1 : 0.03 : 0.24 : 0.74 : 0.06 |
| Parameter | | |
| $\beta, \delta, \delta_1, \delta_2$ | 2.56, 0.11, 1.15, 1.45 | 0.23, 1.88, 3.80, 14.09 |
| $R^2$ | 0.86 | 0.93 |

## IV. CONCLUSION

We have thus developed a quantitative understanding of DEA to sulfur dioxide molecules for resonance peaks at 5.2 and 7.5 eV. We give clear evidence for the presence of one negative-ion resonant state $A_1$ for 5.2-eV resonance and two negative-ion resonant states $A_1 + B_2$ for 7.5-eV resonance based on the angular distribution data.

## ACKNOWLEDGMENTS

[1] E. Illenberger and J. Momigny, *Gaseous Molecular Ions: An Introduction to Elementary Processes Induced by Ionization*, Vol. 2 (Springer Science & Business Media, Springer, New York, 2013).

[2] B. Boudaïffa, P. Cloutier, D. Hunting, M. A. Huels, and L. Sanche, Science **287**, 1658 (2000).

[3] V. S. Prabhudesai, A. H. Kelkar, D. Nandi, and E. Krishnakumar, Phys. Rev. Lett. **95**, 143202 (2005).

[4] I. M. Cadez, V. M. Pejcev, and M. V. Kurepa, J. Phys. D: Appl. Phys. **16**, 305 (1983).

[5] O. J. Orient and S. K. Srivastava, J. Chem. Phys. **78**, 2949 (1983).

[6] J. Rademacher, L. G. Christophorou, and R. P. Blaunstein, J. Chem. Soc., Faraday Trans. 2 **71**, 1212 (1975).

[7] E. Krishnakumar, S. V. K. Kumar, S. A. Rangwala, and S. K. Mitra, J. Phys. B **29**, L657 (1996).

[8] J. McConkey, C. Malone, P. Johnson, C. Winstead, V. McKoy, and I. Kanik, Phys. Rep. **466**, 1 (2008).

[9] D. A. Rallis and J. M. Goodings, Can. J. Chem. **49**, 1571 (1971).

[10] E. Krishnakumar, S. V. K. Kumar, S. A. Rangwala, and S. K. Mitra, Phys. Rev. A **56**, 1945 (1997).

[11] M. Vinodkumar, C. Limbachiya, A. Barot, and N. Mason, Phys. Rev. A **86**, 012706 (2012).

[12] S. M. Spyrou, I. Sauers, and L. G. Christophorou, J. Chem. Phys. **84**, 239 (1986).

[13] M. Gupta and K. L. Baluja, Phys. Rev. A **73**, 042702 (2006).

[14] K. Gope, V. S. Prabhudesai, N. J. Mason, and E. Krishnakumar, J. Chem. Phys. **147**, 054304 (2017).

[15] P. Nag and D. Nandi, Phys. Rev. A **91**, 052705 (2015).

[16] A. T. J. B. Eppink and D. H. Parker, Rev. Sci. Instrum. **68**, 3477 (1997).

[17] D. Nandi, V. S. Prabhudesai, E. Krishnakumar, and A. Chatterjee, Rev. Sci. Instrum. **76**, 053107 (2005).

[18] D. Nandi and E. Krishnakumar, Int. J. Mass Spectrom. **289**, 39 (2010).

[19] T. F. O'Malley and H. S. Taylor, Phys. Rev. **176**, 207 (1968).

[20] R. Azria, R. Abouaf, and D. Teillet-Billy, J. Phys. B: At. Mol. Phys. **15**, L569 (1982).

[21] N. B. Ram, Dissociation dynamics in polyatomic molecules due to electron attachment, Ph.D. thesis, Tata Institute of Fundamental Research, 2010.

[22] N. Ruckhaberle, L. Lehmann, S. Matejcik, E. Illenberger, Y. Bouteiller, V. Periquet, L. Museur, C. Desfrançois, and J.-P. Schermann, J. Phys. Chem. A **101**, 9942 (1997).

[23] A. Moradmand, D. S. Slaughter, D. J. Haxton, T. N. Rescigno, C. W. McCurdy, T. Weber, S. Matsika, A. L. Landers, A. Belkacem, and M. Fogle, Phys. Rev. A **88**, 032703 (2013).